Journal of Physics: Conference Series **2934** (2025) 012022 doi:10.1088/1742-6596/2934/1/012022

REAL TIME VECTOR MAGNETOMETRY WITH QUANTUM DIAMOND SENSOR

Napoom Thooppanom[1], Rapeephat Yodsungnoen[2], Natakorn Sapermsap[1], and Sorawis Sangtawesin[1*]

[1] School of Physics, Institute of Science, Suranaree University of Technology, 111 University Avenue, Muang, Nakhon Ratchasima, 30000, Thailand.
[2] School of Integrated Science and Innovation, Institute of Science, Suranaree University of Technology, 111 University Avenue, Muang, Nakhon Ratchasima, 30000, Thailand.

[*]E-mail: sorawis.s@g.sut.ac.th

Abstract. The magnetic field is fundamental to numerous applications including medical diagnostic, chemical detection, and navigation. Nitrogen vacancy (NV) center in diamond has emerged as a promising quantum system for nanoscale magnetic field sensing, facilitated by a simple optical setup at ambient temperature. Despite advancements, real-time monitoring of the change in local magnetic field and precise determination of field directions remain challenging. Here, we present an approach to real-time vector magnetometry using NV center ensembles. Our system integrates an optical light guide, microwave control, and a graphical user interface (GUI) for controlling the pulse sequence and performing rapid optically detected magnetic resonance (ODMR) measurements. We observe zero-field splitting at 2.87 GHz and the Zeeman effect under external magnetic fields. Additionally, when the magnetic field orientation changes, we can observe multiple transitions from the different NV center axes, from which we can combine with a simulation to determine the vector magnetic field. Our system can be used as a basic quantum phenomena demonstration kit or in applications such as navigation or magnetic field imaging.

1. Introduction

Magnetic field measurement plays a crucial role in human activities such as using magnetic anomaly fields for mapping and navigation, medical diagnosis application such as magnetic resonance imaging (MRI), material characterization with nuclear magnetic resonance (NMR) spectroscopy and studying earth magnetic field in geophysics. Typical examples of magnetic field sensor include hall sensor and magnetoresistive sensor. They have specific properties. The hall sensor uses hall effect or Lorenz force to sense magnetic field with sensitivity 1 T to 10 μT (1). The magnetoresistive sensor consists of giant magnetoresistance (GMR) and anisotropic magnetoresistance (AMR) with sensitivity 0.1 T to 10 nT for GMR and 10 mT to 0.1 nT for AMR (1). While these sensors are effective, they have certain limitations. For example, the output of reed switch indicates only the presence or absence of magnetic field. The hall sensor measures magnetic field strength but only in the perpendicular direction to the sensor. The magnetoresistive sensor measures magnetic field strength but only in the parallel direction to the sensor. For advanced magnetometry, a nitrogen vacancy center (NV) in diamond was discovered in 1960s (2) and found that it had long coherence time (3), good optical properties and accessible two-level systems. As a result, the NV center is a promising quantum system, as it can

simultaneously measure the magnetic field magnitude and direction in ambient conditions (4). For applications, there are attempt to apply NV center to do magnetometry. For example, using NV center in nanodiamond detect directly action potentials (APs) of worm with sensitivity 10 pT/Hz (5). Applying NV-based magnetic microscopy detects magnetic label protein interleukin-6 found at COVID-19 through concentration of magnetic bead in sample (6). For magnetic field imaging, NV center is used to detect magnetic field by quantum diamond microscope with showing label cancer biomarker (7). Additionally, the NV centers can be used in combination with nuclear magnetic resonance (NMR) spectroscopy to detect nanoscale atomic and molecular structures (8, 9, 10). Despite advancements, real-time monitoring of the change is still a challenge, as they have only been demonstrated in the regime with small magnetic field changes (11, 12, 13). Ultimately, we need to develop a high accuracy measurement that can respond to large magnetic field magnitude and orientation changes with a fast response time. There are some approaches to bring NV centers to detect various changes such as global navigation satellite system (GNSS) (14). In this work, we focus to detect local magnetic field using static magnet through NV center in diamond with real-time demonstration. The magnet can change orientation to change magnetic field direction to NV center. Due to changing the orientation, we can study the phenomenon through fluorescence of NV center and compare analysed angle from experimental data with the set angle. In the experimental setup, we use ensemble of NV centers instead of single NV center due to ensemble enhancement. We also developed a sweep function to replace slow frequency set functions.

2. Methodology

Normally, confocal microscopes are used for studying the NV centers in diamond, because it allows high-resolution imaging (15). However, the measurement typically requires a significant amount of time due to the low photon count rate of single NV centers. Here, we use ensemble of NV centers in diamond in a quantum diamond spectrometer (QDS) configuration, as outlined by Bucher et. al (4), as the system provides a stronger fluorescence signal that results in a reduced data acquisition time. The ability to obtain spatial resolution making it well-suited for sensor applications. In our experiments, we use the system to perform optically detected magnetic resonance (ODMR) using our software, and the data is analyzed to determine the direction of the magnetic field.

2.1 Sample

We use ensemble NV center in diamond from Element Six (DNV B14). The diamond is synthesized via chemical vapor deposition (CVD) with the nitrogen concentration of approximately 4.5 ppm. The diamond is cut in size 3 mm x 3 mm with a thickness 0.5 mm, with crystallographic orientation {100} on polished faces.

According to Figure 1c, the energy levels of the NV center consist of ground, excited, and metastable states. The ground and excited states are spin triplet which include the spin projections $m_s = 0$ and degenerate levels $m_s = \pm 1$. For energy level $m_s = 0$, the red fluorescence from the NV center is emitted when the NV center electrons get excited from the ground state ($m_s = 0$) to the excited state ($m_s = 0$) with the green laser and relax to the ground state, following the spin selection rule (16). This red fluorescence corresponds to zero phonon line of the NV center at 637 nm (17, 18). For energy levels $m_s = \pm 1$, after excitation, the electrons can either relax normally following the spin selection rule to ground state $m_s = \pm 1$ and emit red fluorescence, or the electrons can non-radiatively relax through metastable state. This metastable path can reduce

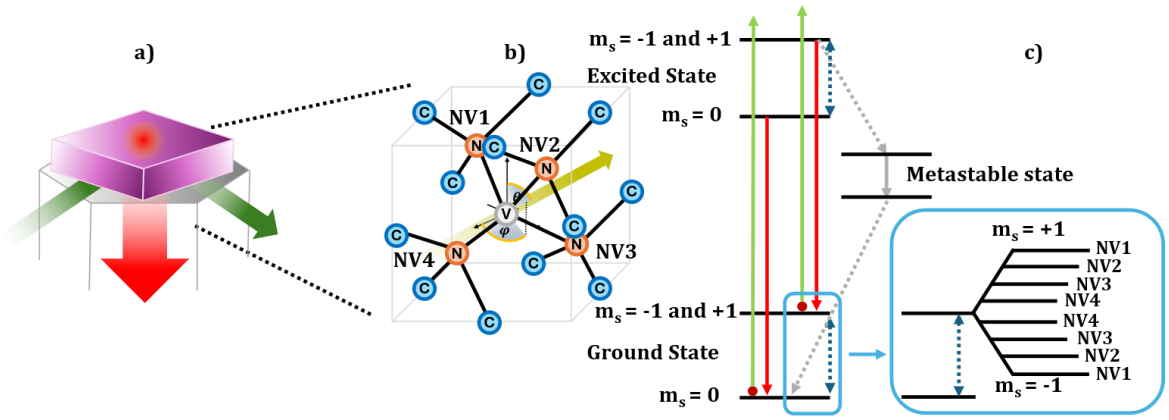

Figure 1. (a) the diamond is illuminated with a green laser and emit red fluorescence. (b) The NV center defect structure in diamond that occurs from the replacement of two carbon atoms with a nitrogen atom and a vacancy. The NV centers can exist in 4 different orientations along the diamond lattice. Each NV orientation can experience different effects from the magnetic field, allowing the determination of the magnitude and direction of the magnetic field. (c) Energy level of NV center. The NV ground state is a triplet consisting of state $m_s = 0$ and degenerate states $m_s = \pm 1$. Following the selection rule, electron transitions between the ground state and excited state should preserve the spin state and emit fluorescence photons. However, electrons in the excited states $m_s = \pm 1$ have probabilities to transition to a metastable state and non-radiatively return to the ground state at $m_s=0$. When the external magnetic field is added to the NV center, the degenerate states can separate via Zeeman splitting, depending on the magnitude and direction of the magnetic field.

the fluorescence signal contrast. Therefore, the interactions of NV center can be studied using fluorescence detection.

To understand the NV center, we use the following Hamiltonian to describe the NV center under the effect of an external magnetic field (17–19)

$$H = DS_Z^2 - \gamma_{NV}\vec{B} \cdot \vec{S}. \qquad \text{Eq. 1}$$

Here, H is the Hamiltonian of the NV center, D is the zero-field splitting parameter, $\vec{S}$ is the vector spin operator, γ_{NV} is the gyromagnetic ratio, and $\vec{B}$ is the magnetic field vector. This Hamiltonian consists of two terms: the first term represents zero-field splitting, which is independent of the external magnetic field, while the second term represents Zeeman splitting, which includes the interaction of the magnetic field with the NV center. The degenerate levels $m_s = \pm 1$ of the NV

center can be splitted by a linear factor of $2\gamma_{NV}B_z$ when the external magnetic field is aligned with the NV center, while a misaligned magnetic field results in smaller, non-linear splitting patterns. These non-linear patterns have four possible variations due to crystallographic factors, resulting in four pairs of possible energy levels.

2.2 Quantum diamond spectrometer

In this work, we use the quantum diamond spectrometer design outlined by Bucher et. al (4). The system consists of an optical system and electronics system, as shown in figure 2a.

2.2.1 Optical system

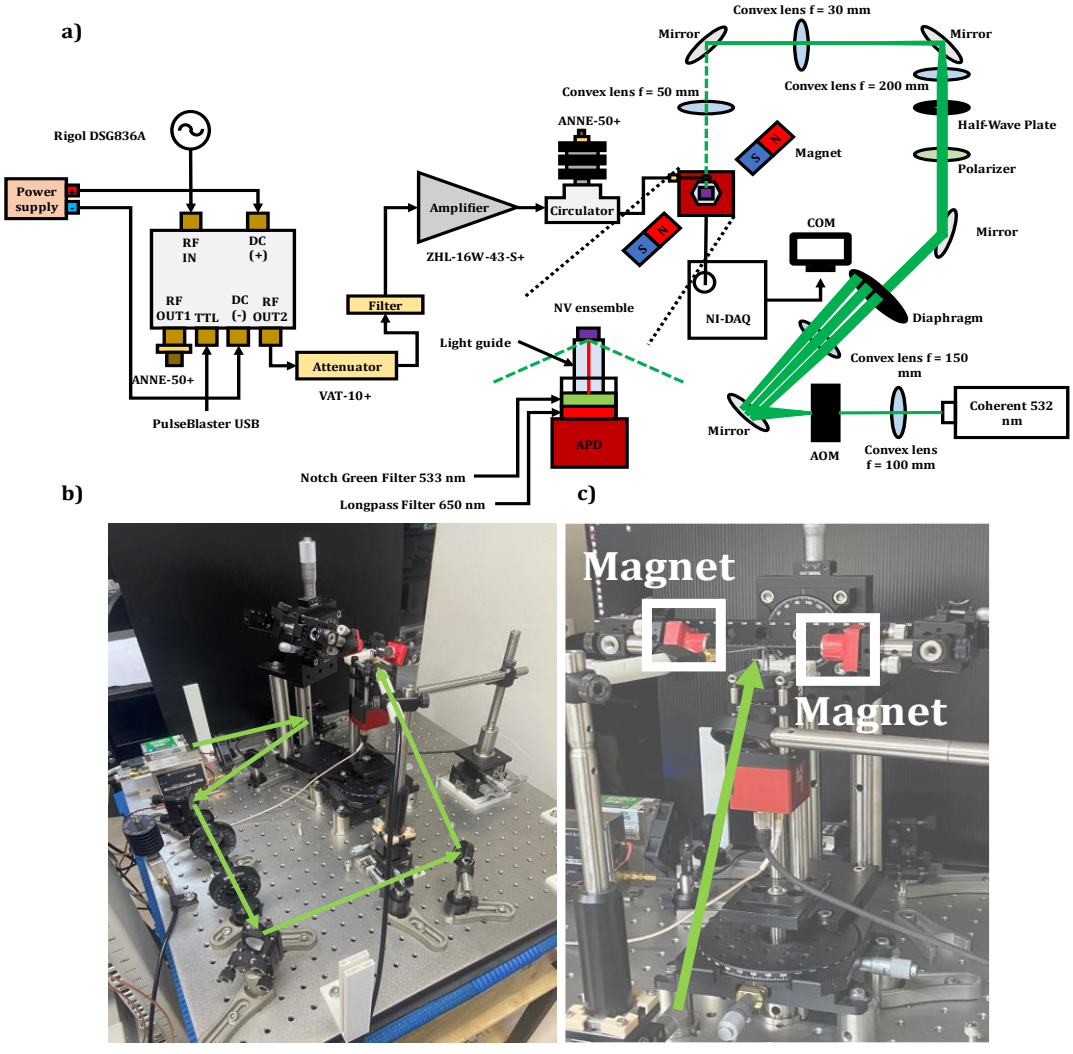

Figure 2. (a) Quantum diamond spectrometer schematic consists of optical system and electronics system. (b) Optical part of quantum diamond spectrometer. (c) The laser path (green line) goes to the diamond on top of light guide. The magnets (white boxes) can be arranged in different directions with respect to the diamond.

The experimental setup is shown in figure 2b. The optical system starts from 532-nm green laser source (Coherent OBIS 532). The laser is focused by convex lens (f = 100 mm) (Thorlabs AC254-100-A) to pass through an acousto-optic modulator (AOM, Gooch & Housego AOMO 3080-120). The AOM creates a diffraction pattern, and we use a diaphragm (Thorlabs ID37Z) to choose the first order diffraction that can be turned on and off for ODMR measurements. The first order beam then goes through a polarizer (Thorlabs LPVISE 100-A) and a half-wave plate (Thorlabs WPH05M-532) to control the polarization (20). The polarized beam is demagnified by two convex lenses (f = 200 mm and f = 30 mm) (Thorlabs AC254-200-A and Thorlabs AC254-030-A). Then, the laser beam is directed upward to the diamond that is placed on an optical light guide (49-402, Edmund optics), as shown in figure 2c. The laser is finally focused by a convex lens (f = 50 mm, Thorlabs LA4148). The red fluorescence emission from the diamond is collected through the light guide into an avalanche photodetector (APD, Laser components A-CUBE-S3000-03). We place a notch and long-pass filters (Thorlabs NF533-17 and Thorlabs FELH0600) before the APD to remove the remaining excitation. Then, the APD signal is sent to a data acquisition card (National Instruments PCIe-6363) for data processing by computer.

2.2.2 Electronics system

As shown in figure 2a, the electronic system generates microwave signals through a microwave loop placed on top of the diamond. The microwave (MW) signal is initially generated by a signal generator (RIGOL DSG836A) and then sent as an into an RF IN port of a microwave switch (ZASWA-2-50DRA+). The state of the switch is controlled by a timing sequencer (PulseBlaster ESR-Pro500) via a transistor-transistor logic (TTL) signal. Upon receiving a TTL HI signal, the switch passes the MW signal to the OUT2 port, where it is subsequently filtered (VHF-1600+) and attenuated (VAT-10A+) before reaching the amplifier (Mini-Circuits ZHL-16W-43S+). The amplified signal is then sent to the microwave loop through a circulator (Ditom D3C2040) to prevent signal reflection.

3. Experiment Software

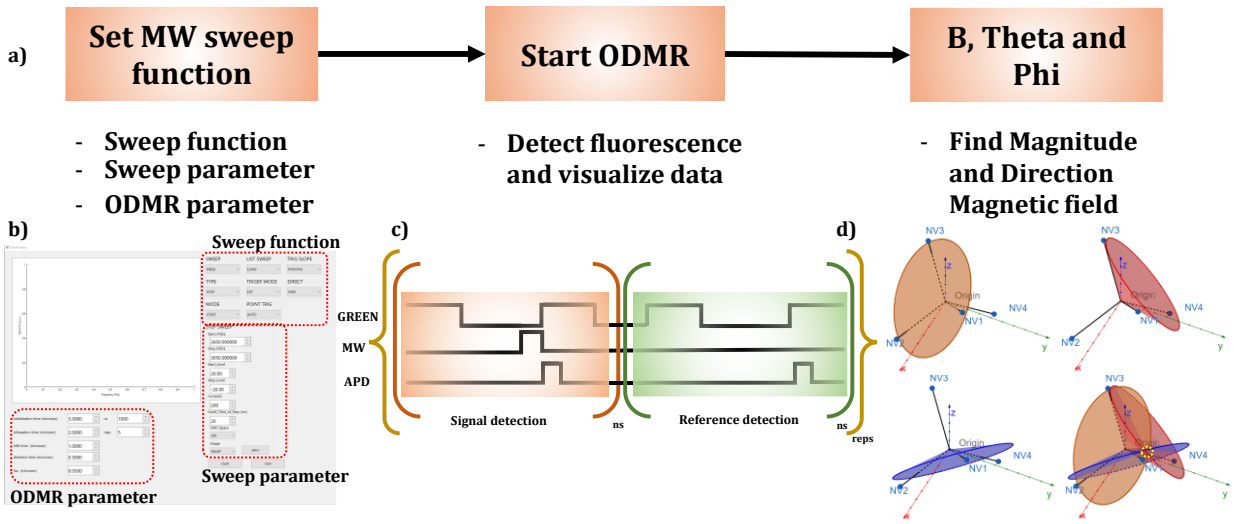

Figure 3. (a) Workflow of the system. we start to define sweep function, sweep parameters and ODMR parameter. (b) Graphical user interface of the system. (c) Pulse sequence for ODMR experiment. (d) Illustration of magnetic field direction determination process (21).

In this work, graphical user interface (GUI) software is developed to perform real-time ODMR measurements. This software can graphically illustrate the ODMR plot, while allowing separate analysis of the direction of the magnetic field. Users can adjust the sweep function, sweep parameters, and ODMR parameters through the software, which is separated into three main parts:

3.1 Sweep program

The sweep program relays the command to the corresponding sweep function of the microwave signal generator, generating a linear series of frequencies or powers as defined by the user through the sweep parameters. The ODMR parameter defines the experimental settings, such as exposure time, relaxation time, and acquisition time.

3.2 Optically Detected Magnetic Resonance (ODMR) Experiment

ODMR is an integration of electron spin resonance (ESR) and optical measurements showing the relationship between optical measurement and microwave frequency. As shown in the figure 3c, ODMR pulse sequence includes 532-nm laser pulse ("Green"), microwave pulse ("MW"), data acquisition trigger ("APD"). The sequence starts with "Green" turning the laser on for NV polarization. After this, the laser is turned off, allowing the NV center to relax to the ground state. Following relaxation, the microwave is turned on to manipulate the electron spin states. Next, we turn on the "Green" again detect the signal. We repeat this experiments for "n" rounds for averaging out the noise. Then, we repeat the entire process all over again, without the application of microwave, as a reference signal. The data from the signal and reference detections are then divided to obtain the photoluminescence (PL) signal.

3.3 Calculation of magnitude and direction of magnetic field

The Zeeman splitting data is collected from the ODMR experiment. The data is then analysed to fit the frequencies of each dip in the spectrum. Subsequently, we use a simulation program to define the NV axes corresponding to each fitting dips in the splitting. The defined NV axes and the fitted frequencies are used to calculate the magnetic field magnitude by eq. 2 (21, 22).

$$B = \frac{\sqrt{(w_1^2 + w_2^2 - w_1 w_2 - D^2)/3}}{\gamma_{NV}}, \qquad \text{Eq. 2}$$

where B is the magnetic field magnitude, w_1 and w_2 are the frequency pair of Zeeman splitting, D is zero field splitting and γ_{NV} is gyromagnetic ratio. After calculating the magnetic field magnitude, we continue to calculate magnetic field direction. The magnetic field angle is determined by finding the angle between a NV center and the magnetic field using the eq. 3 (21, 22).

$$\alpha = \arccos\left(\pm \sqrt{\frac{(2w_1 - w_2 - D)(w_1 - 2w_2 + D)(w_1 + w_2 + D)}{[9D({w_1}^2 - w_1 w_2 + {w_2}^2 - D^2)]}} \right). \qquad \text{Eq. 3}$$

The angle obtained from this calculation represents the direction of the magnetic field along one NV axis. This angle is then used to define a cone swept along the NV axis where the magnetic field's magnitude is constant on the surface and border of this cone. From each NV axes, the cone represents magnetic field area and their intersection represents the true magnetic field direction in the laboratory reference frame. This method allows for determining the precise direction and magnitude of the magnetic field.

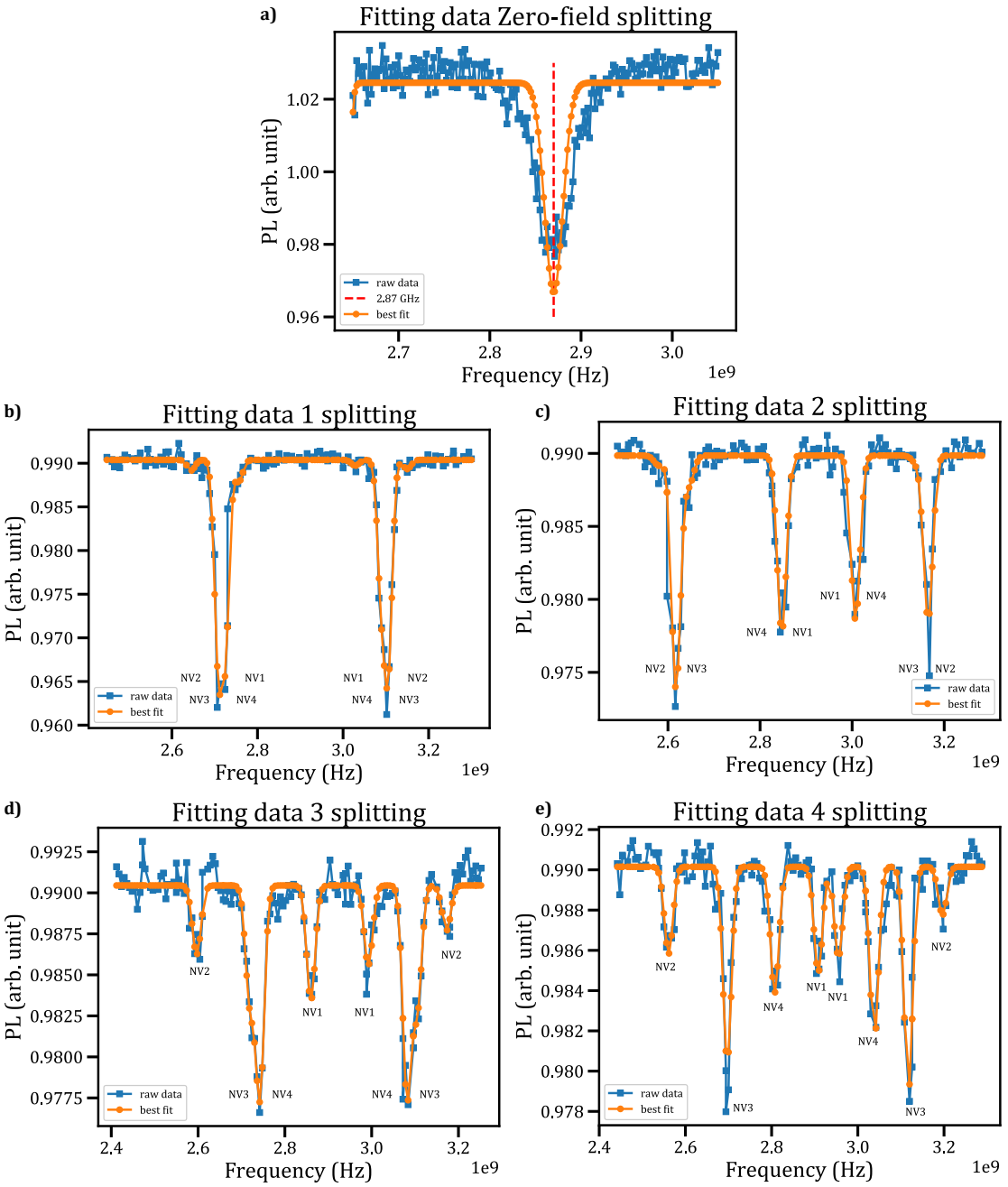

Figure 4. (a) Zero-field splitting at 2.87 GHz (b-e) Type of Zeeman splitting patterns for magnetic field act on each NV axes like in figure 1b. When magnetic field direction acts more than a NV axis, Changing of Zeeman splitting pattern depends on number of NV axes sensing to magnetic field.

4. Result and discussion

The ODMR measurement illustrates the fluorescence contrast that can be used to determine the magnitude and direction of the magnetic field. In the absence of an external magnetic field, the ODMR signal always shows a single dip with reduced contrast (figure 4a), corresponding to the electrons in the degenerate levels $m_s = \pm 1$. When an external magnetic field is present along the (100) direction of the crystal, the four NV axes are degenerate, and the ODMR signal shows only one splitting in figurer 4b. When the magnetic field is not aligned with the crystallographic axis or an NV axis, up to four splittings can be observed like figure 4c-4e, depending on the angle.

The separation between these splittings indicates the influence of the magnetic field on the NV center. As shown in Table 1, four experimental conditions were tested to demonstrate the system's performance in determining the magnetic field direction from ODMR data consisting of one, two, three, and four splittings. The set angle was determined by the rotation stage position, while the calculated angle was determined using Eq. 3 with w_1 and w_2 obtained by fitting the ODMR data with a four-Gaussian model. When we collected both angles, we compare difference, data in bracket, of them to analyse error from calculated angles. As a result in Table 1, the calculated values showed a similar trend to the set values. However, significant angle differences were observed in the cases of 1, 2, and 3 splittings . The reasons of the discrepancies of angle are possibly due to the orientation of diamond and some overlapped transitions.

Here, we attribute the large angle discrepancies from the set angle to be a result of the misalignment of the diamond sample with respect to the moving magnets. Specifically, we use a [100] diamond placed on top of an optical light guide and orient the magnet translation stages around the top of the light guide. Any misalignments of the xy and z positions of the system can contribute to a systematic offset to the measured angle. Furthermore, for overlapping transitions, it is difficult to identify exact positions of the degenerate transitions and thus the error can propagate into the magnetic field angle determination.

Table 1. Comparison between the magnetic field direction, indicated by θ and ϕ angles (Figure 1B), from settings angles and calculation angles.

Splitting	Setting angle (degrees)		Calculated angle (degrees)	
	θ	ϕ	θ	ϕ
1	94	174	87.4 (-6.6)	179.2 (+5.2)
2	66	174	61.9 (-4.1)	177.3 (+3.3)
3	80	155	72.6 (-7.4)	164.5 (+9.5)
4	64	155	59.7 (-4.3)	162 (+7)

The smallest angle discrepancy was detected in case of 4 splittings, as the levels are non-degenerate. This angle discrepancy can be improved by better alignment of the diamond and of the stage center of rotation with respect to the diamond. For the real time measurement, we can run sweep program 100 points in 5 seconds, limited by the 20-ms dwell time of the microwave source. This limitation can be overcome by adding a low-frequency signal generator and a mixer for frequency sweeps.

5. Conclusion

We can demonstrate the use of NV center for magnetic field detection. The NV center can specify direction of magnetic field. The calculated value of magnetic field direction is close to the experimental settings. The accuracy of the magnetic field direction can be further improved by adjusting the fitting method and recalibrating the diamond position. In the future, we expect that we can define direction of magnetic field from far away and create magnetic fields image from vector.

Acknowledgments

This research has received funding support from the NSRF via the Program Management Unit for Human Resources & Institutional Development, Research and Innovation [grant number B39G670018]. Napoom Thooppanom has received financial support from the Development Promotion of Science and Technology (DPST) scholarship.

References

1. Herrera-May AL, Aguilera-Cortés LA, García-Ramírez PJ, Manjarrez E. Resonant magnetic field sensors based on MEMS technology. Sensors. 2009;9(10):7785-813.

2. Dyer H, Raal F, Du Preez L, Loubser J. Optical absorption features associated with paramagnetic nitrogen in diamond. Philosophical Magazine. 1965;11(112):763-74.

3. Ma Y, Chen J, Wang C. Growth of Diamond Thin Film and Creation of NV Centers. Applications and Use of Diamond: IntechOpen; 2022.

4. Bucher DB, Aude Craik DP, Backlund MP, Turner MJ, Ben Dor O, Glenn DR, et al. Quantum diamond spectrometer for nanoscale NMR and ESR spectroscopy. Nature Protocols. 2019;14(9):2707-47.

5. Barry JF, Turner MJ, Schloss JM, Glenn DR, Song Y, Lukin MD, et al. Optical magnetic detection of single-neuron action potentials using quantum defects in diamond. Proceedings of the National Academy of Sciences. 2016;113(49):14133-8.

6. Atallah J, Archambault D, Randall JD, Shepro A, Styskal LE, Glenn DR, et al. Rapid quantum magnetic IL-6 point-of-care assay in patients hospitalized with COVID-19. Diagnostics. 2022;12(5):1164.

7. Glenn DR, Lee K, Park H, Weissleder R, Yacoby A, Lukin MD, et al. Single-cell magnetic imaging using a quantum diamond microscope. Nature methods. 2015;12(8):736-8.

8. DeVience SJ, Pham LM, Lovchinsky I, Sushkov AO, Bar-Gill N, Belthangady C, et al. Nanoscale NMR spectroscopy and imaging of multiple nuclear species. Nature nanotechnology. 2015;10(2):129-34.

9. Bucher DB, Glenn DR, Park H, Lukin MD, Walsworth RL. Hyperpolarization-enhanced NMR spectroscopy with femtomole sensitivity using quantum defects in diamond. Physical Review X. 2020;10(2):021053.

10. Arunkumar N, Bucher DB, Turner MJ, TomHon P, Glenn D, Lehmkuhl S, et al. Micron-scale NV-NMR spectroscopy with signal amplification by reversible exchange. PRX quantum. 2021;2(1):010305.

11. Schoenfeld RS, Harneit W. Real time magnetic field sensing and imaging using a single spin in diamond. Physical review letters. 2011;106(3):030802.

12. Turner E, Wu S-H, Li X, Wang H. Real-Time Magnetometry Using Dark States of a Nitrogen Vacancy Center. arXiv preprint arXiv:211109943. 2021.

13. Liu Z, Zheng D, Fu J, Tang C, Liu Y, Wang H, et al. Integrated NV (Nitrogen Vacancy) Vector Magnetometer in Real-time Utilizing Frequency-hopping Method. IEEE Sensors Journal. 2024.

14. Wang X, Li W, Moran B, Gibson B, Hall L, Simpson D, et al. Quantum diamond magnetometry for navigation in gnss denied environments. Gravity, Positioning and Reference Frames. 2022:87.

15. Sangtawesin S, Dwyer BL, Srinivasan S, Allred JJ, Rodgers LVH, De Greve K, et al. Origins of Diamond Surface Noise Probed by Correlating Single-Spin Measurements with Surface Spectroscopy. Physical Review X. 2019;9(3):031052.

16. Maze JR, Gali A, Togan E, Chu Y, Trifonov A, Kaxiras E, et al. Properties of nitrogen-vacancy centers in diamond: the group theoretic approach. New Journal of Physics. 2011;13(2):025025.

17. Jelezko F, Wrachtrup J. Single defect centres in diamond: A review. physica status solidi (a). 2006;203(13):3207-25.

18. Doherty MW, Manson NB, Delaney P, Jelezko F, Wrachtrup J, Hollenberg LCL. The nitrogen-vacancy colour centre in diamond. Physics Reports. 2013;528(1):1-45.

19. Childress L, Gurudev Dutt MV, Taylor JM, Zibrov AS, Jelezko F, Wrachtrup J, et al. Coherent dynamics of coupled electron and nuclear spin qubits in diamond. Science. 2006;314(5797):281-5.

20. Alegre TPM, Santori C, Medeiros-Ribeiro G, Beausoleil RG. Polarization-selective excitation of nitrogen vacancy centers in diamond. Physical Review B. 2007;76(16).

21. Chen B, Hou X, Ge F, Zhang X, Ji Y, Li H, et al. Calibration-Free Vector Magnetometry Using Nitrogen-Vacancy Center in Diamond Integrated with Optical Vortex Beam. Nano Lett. 2020;20(11):8267-72.

22. Balasubramanian G, Chan IY, Kolesov R, Al-Hmoud M, Tisler J, Shin C, et al. Nanoscale imaging magnetometry with diamond spins under ambient conditions. Nature. 2008;455(7213):648-51.